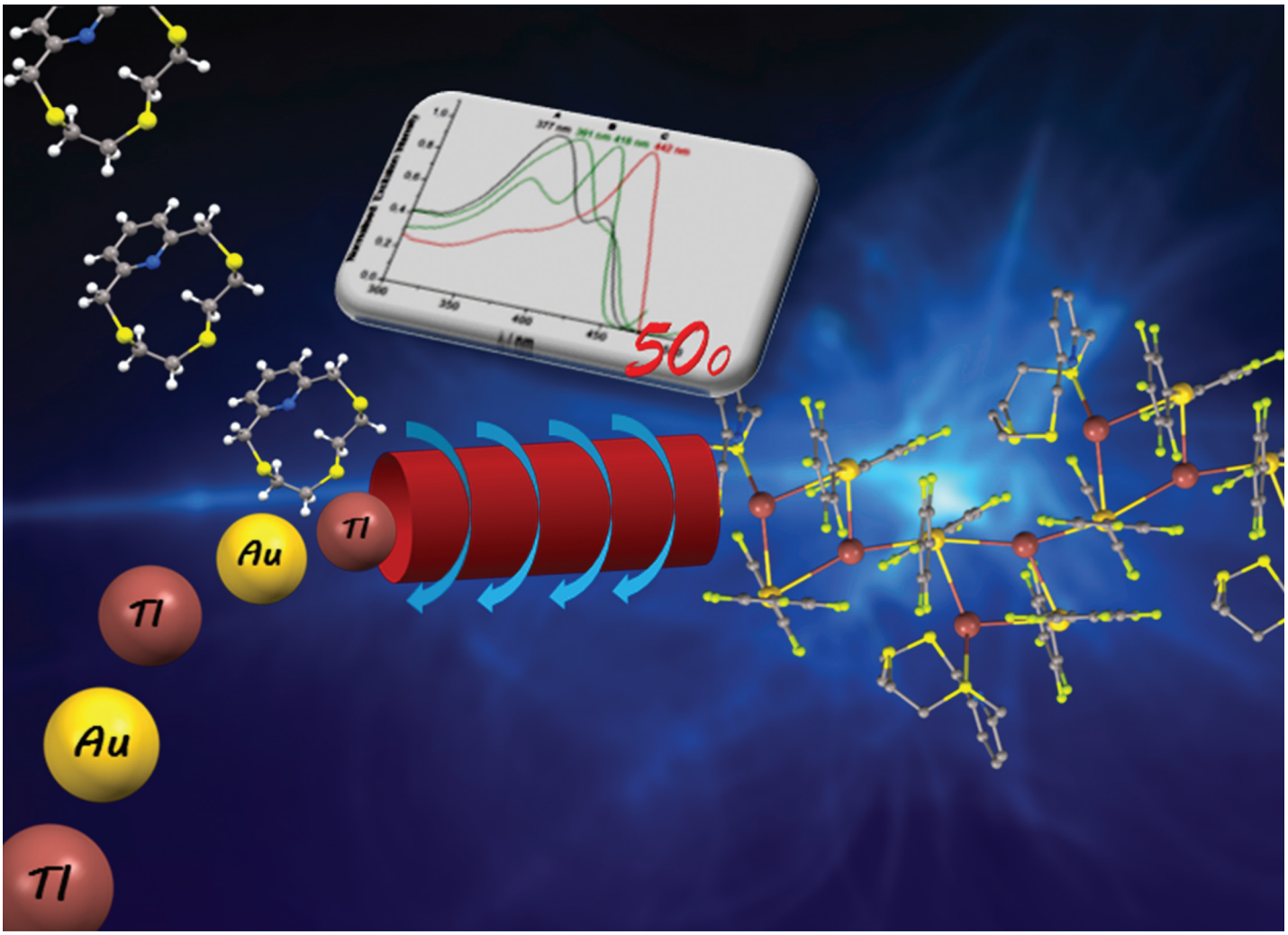

Showcasing research from Professor Lippolis's laboratory, University of Cagliari, Italy and Prof. M. Concepción Gimeno, Instituto de Síntesis Química y Catálisis Homogénea (ISQCH), CSIC-Universidad de Zaragoza, Spain.

Luminescent gold–thallium derivatives with a pyridine-containing 12-membered aza-thioether macrocycle

A heterometallic Tl–Au compound containing the ligand 2,5,8-trithia[9](2,6)pyridinophane displays a thermochromic luminescence due to MM′CT transitions.

As featured in:

See Vito Lippolis, M. Concepción Gimeno *et al.*, *Dalton Trans.*, 2021, **50**, 9709.

ROYAL SOCIETY OF CHEMISTRY

rsc.li/dalton

Registered charity number: 207890

Dalton Transactions

ROYAL SOCIETY OF CHEMISTRY

PAPER

View Article Online
View Journal | View Issue

Open Access Article. Published on 15 June 2021. Downloaded on 1/21/2026 2:17:31 AM.
This article is licensed under a Creative Commons Attribution-NonCommercial 3.0 Unported Licence.

Check for updates

Cite this: *Dalton Trans.*, 2021, **50**, 9709

Luminescent gold–thallium derivatives with a pyridine-containing 12-membered aza-thioether macrocycle†

Francesco Caddeo,[a] Vanesa Fernández-Moreira,[a] Massimiliano Arca,[b] Anna Pintus,[b] Antonio Laguna,[a] Vito Lippolis *[b] and M. Concepción Gimeno *[a]

The coordination modes of the ligand 2,5,8-trithia[9](2,6)pyridinophane (**L**) to thallium(I), gold(III) and gold (I) have been studied. Thallium(I) is coordinated by the macrocyclic ligand in [Tl(L)](PF_6) (**1**) through all the sulfur and nitrogen atoms, in a distorted square-pyramidal geometry with the thallium(I) ion in the apical position and with the presence of an inert lone pair. Gold(III) is bonded by the ligand only through the nitrogen of the pyridine group in [$AuCl_3$(L)] (**2**), whereas two Au^I–C_6F_5 fragments coordinate the sulfur atoms next to the pyridine moiety of the ligand in [{$Au(C_6F_5)$}$_2$(μ-L)] (**3**), which form a linear polymer through intermolecular aurophilic contacts. The heterometallic Tl^I/Au^I complex {[$Au(C_6F_5)_2Tl]_2$(L)}$_n$ (**4**) features a polymeric structural nature with a metallic pseudo-rhombic Au_2Tl_2 core, which repeats itself forming a zig-zag polymer. In each Au_2Tl_2 unit only one thallium atom is bonded by the NS_3 donor set of the macrocyclic ligand and also forms two unsupported Au–Tl bonds with two [$Au(C_6F_5)_2$]$^-$ units in an overall pseudo-octahedral geometry. The other thallium atom similarly bridges the same [$Au(C_6F_5)_2$]$^-$ units and links a neighbouring Au_2Tl_2 moiety, thus exhibiting a distorted trigonal planar geometry being bonded only to three gold atoms with unsupported Au–Tl interactions. This complex displays an interesting thermochromic behaviour showing emissions mainly resulting from MM'CT transitions at room temperature. At 77 K a dual emission appears, probably arising from the two different thallium environments. DFT calculations have been carried out in the attempt to investigate the origin of the emissions of complex **4**.

Received 17th May 2021,
Accepted 11th June 2021

DOI: 10.1039/d1dt01599k

rsc.li/dalton

Introduction

The luminescence properties of heteronuclear gold(I) complexes featuring $Au^I\cdots Au^I$ and/or $Au^I\cdots M$ metallophilic interactions [M = transition and post-transition closed-shell metal ions such as Ag^I, Cu^I and Tl^I][1–10] are currently considered of great interest not only from a theoretical point of view[11–13] but also for their potential applications.[14–25] A great number of factors contribute to affect the photophysical properties of these compounds, making a rational structure–property design a very challenging task. However, the nature of the organic ligands used to support metallophilic interactions is fundamental in controlling the nuclearity of these complexes, the intermolecular interaction patterns based on $Au^I\cdots M$ interactions in the crystal lattice, and, therefore, the optical properties.

Recently, we have proved the great versatility and potentiality of aza-[26] and thioether crowns of different size,[27,28] aliphatic mixed thia-aza macrocycles of different nature/number of donors atoms[29,30] and their pendant arm derivatives[30–32] in supporting $Au^I\cdots M^I$ [M = Ag, Tl] metallophilic interactions for the formation of heteronuclear gold(I) complexes featuring unusual structural archetypes and optical properties.

The presence of rigid moieties in the macrocyclic structure of the ligand used to support metallophilic interactions might represent a further parameter to consider for fine-tuning the structural and photophysical properties of heteronuclear gold(I) complexes built *via* intra- and intermolecular $Au^I\cdots M$ interactions.

While mixed donor macrocycles featuring rigid heterocyclic moieties, such as pyridine (py) and 1,10-phenanthroline (phen) as integral parts of the macrocyclic structure, have been employed as efficient and selective ionophores in solid-phase extraction, selective transport, preparation of PVC-based ion-selective electrodes, and fluorimetric chemosensors for

[a]*Departamento de Química Inorgánica, Instituto de Síntesis Química y Catálisis Homogénea (ISQCH), CSIC-Universidad de Zaragoza, 50009 Zaragoza, Spain. E-mail: gimeno@unizar.es*
[b]*Dipartimento di Scienze Chimiche e Geologiche, Università degli Studi di Cagliari, S.S. 554 Bivio per Sestu, 09042 Monserrato, CA, Italy. E-mail: lippolis@unica.it*

† Electronic supplementary information (ESI) available: Emission and excitation spectra, NMR spectra and DFT data. CCDC 2083080–2083082. For ESI and crystallographic data in CIF or other electronic format see DOI: 10.1039/d1dt01599k

Open Access Article. Published on 15 June 2021. Downloaded on 1/21/2026 2:17:31 AM.
This article is licensed under a Creative Commons Attribution-NonCommercial 3.0 Unported Licence.

some transition and heavy metal ions,[33–35] their use in the development of heteronuclear fluorescent complexes has been only marginally tapped.[32,36]

Here we report the results of our investigation on the coordination chemistry of the tetradentate macrocycle 2,5,8-trithia[9](2,6)-pyridinophane (**L**) to thallium(I), gold(I) and gold (III) ions and its use in the formation of luminescent heteronuclear Au^I/Tl^I complexes.

The few information available on the coordination chemistry of **L**[37] (only the X-ray crystal structure of the following complexes are known: $[Ag(L)]_n(CF_3CO_2)_n{\cdot}nH_2O$,[38] $[Ag(L)]_n(NO_3)_n$,[39] $[Cu(L)](NO_3)_2$,[38] $[Hg(L)Cl]NO_3$[40] and $[Ni_2(L)_2Cl_2](BF_4)_2{\cdot}1.5MeNO_2$[41]) point out a folded conformation assumed by the ligand upon coordination, as a consequence of a conformational constrain on the aliphatic portion of the ring exerted by the rigid heteroaromatic moiety. This notwithstanding, tetracoordination of **L** to a metal centre is possible with the coordination sites left free for further interactions. These properties can be useful factors in expanding the scope of forcing unusual structural archetypes and metal ion arrangements in Au^I/Tl^I heteronuclear complexes featuring metallophilic interactions.

Results and discussion

Synthesis and characterisation

The ligand **L** was prepared by reaction of 2,6-di(chloromethyl) pyridine with 2,2-thiodi(ethanethiol).[42] The crystal structure of **L** was previously reported:[43] the aliphatic chain of the ring is tilted over the plane containing the pyridine unit, presumably because of the repulsion between the two sulfur atoms close to the aromatic ring.[44] The other sulfur atom adopts an exodentate orientation with the lone pairs of electrons (LPs) pointing out of the ring cavity. Therefore, a conformational change is required to coordinate the metal centre with all four donor atoms.

The synthesis of the thallium(I), gold(III), and gold(I) complexes **1–3** was accomplished by reaction of **L** with the metal salt precursors $TlPF_6$, $AuCl_3{\cdot}nH_2O$ and $[Au(C_6F_5)(tht)]$ (tht = tetrahydrothiophene), respectively (see Scheme 1).

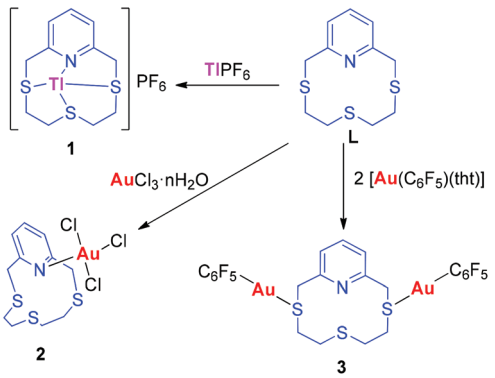

Scheme 1 Synthesis of thallium and gold complexes **1–3**.

The characterization of each complex was performed using mass spectrometry, FT-IR, ^1H, ^{13}C NMR, and when appropriate ^{19}F NMR spectroscopy, and the data suggest for them the formulation reported in Scheme 1. FT-IR data clearly show some absorptions corroborating the formation of the coordination compounds. **1** shows the ν(P–F) stretching band at 827 cm^{-1} corresponding to the PF_6^- anionic group. Complex **2** presents two close ν(Au–Cl) stretching bands at around 333 cm^{-1}, which point to the presence of more than one chlorido ligand coordinated to the gold(III) centre. In complex **3** the typical absorptions of the pentafluorophenyl group bound to gold(I) appear at *ca.* 1505, 955 and 800 cm^{-1}. In addition, ^1H, ^{13}C and ^{19}F NMR spectroscopy supports the proposed formulation for these complexes (see Fig. S1–S4 in the, ESI†). These experiments were carried out in different deuterated solvents due to low solubility of the compounds; therefore, a direct comparison between them is sometimes difficult. ^1H NMR spectra of complexes **1** and **2** were performed in CD_2Cl_2 and $(CD_3)_2CO$, respectively, and displayed two broad singlets at 2.95 and 2.61 ppm and 2.85 and 2.75 ppm, respectively, assigned to the crown thioether protons (–SCH_2CH_2S–). An additional singlet also appears due to the methylene protons adjacent to the pyridine (–SCH_2Py) at 4.17 and 4.59 ppm for **1** and **2**, respectively (Table 1). For complex **1**, there is a pronounced downfield shift in comparison with the signals of the free ligand, suggesting that the coordination of the metal centre to the sulfur atoms has taken place and is retained in solution. Interestingly, no AB spin system is observed for the signals corresponding to the methylene protons next to the pyridine ring as observed for the 1 : 1 complexes of **L** with Pd^{II}, Pt^{II} and Rh^{III}.[37] For compound **2** the shift is more noticeable for the protons adjacent to the pyridine group and those of the pyridine fragment, which display a pronounced chemical shift compared to the free ligand (from 7.42 and 7.85 ppm to 8.22 and 8.76 ppm) suggesting that the coordination of the gold(III) metal centre by the pyridine nitrogen donor atom occurs and it is retained in solution. Since all the methylene groups within the ligand are equivalent, a coordination of the $AuCl_3$

Table 1 Relevant ^1H NMR signals and MS peaks recorded for complexes **1–4**

	^1H (ppm)[d] (–SCH_2CH_2S–)	^1H (ppm)[e] (–SCH_2Py)	m/z[f]
1[a]	2.95 (4H, s_{br}) 2.61 (4H, s_{br})	4.17 (4H, s)	462.0 $[(LTl)^+]$
2[b]	2.85 (4H, s_{br}) 2.75 (4H, s_{br})	4.59 (4H, s)	454.2 $[(M - 3Cl)^+]$
3[a]	3.69 (2H, s_{br}) 3.25 (4H, s_{br}) 2.95 (2H, s_{br})	4.55 (1H, s_{br}) 4.39 (2H, s_{br}) 4.05 (1H, s_{br})	817.9 $[(M - C_6F_5)^+]$
4[c]	2.69–2.36 (8H, m)	3.92 (4H, s)	867.6 $[(M + CH_3CN - TlAu(C_6F_5)_3)^+]$
L[g]	2.53 (8H, s)	3.85(4H, s)	

[a] NMR spectra measured in CD_2Cl_2. [b] NMR spectra measured in $(CD_3)_2CO$. [c] NMR spectra measured in CD_3OD. [d] ^1H NMR signal for the protons –SCH_2CH_2S–. [e] ^1H NMR signal for the protons –SCH_2Py. [f] MS(MALDI$^+$). [g] NMR spectra measured in $CDCl_3$. s_{br} = broad singlet.

Open Access Article. Published on 15 June 2021. Downloaded on 1/21/2026 2:17:31 AM.
This article is licensed under a Creative Commons Attribution-NonCommercial 3.0 Unported Licence.

moiety to only the nitrogen atom of the pyridine is proposed (see Scheme 1). Complex **3** presents a completely different pattern of signals in the ^{1}H NMR spectrum recorded in CD_2Cl_2 (Table 1).

In particular, complex **3** exhibits two sets of three broad bands integrating for 2 : 4 : 2 and 1 : 2 : 1 protons for the crown thioether portion and the methylene protons adjacent to the pyridine, respectively (see Table 1 for the chemical shifts values). All of them shifted to lower field upon coordination with respect to the free ligand.

The synthesis of the heterometallic Au^I/Tl^I complex **4** was achieved by reaction of the ligand **L** with $TlPF_6$ and $NBu_4[Au(C_6F_5)_2]$ (see Scheme 2). The structure in the solid state indicates a 1 : 2 : 2 **L** : Tl : Au ratio (see X-ray data below), but NMR data do not provide conclusive information about the solution structure (Table 1). The ^{1}H NMR spectrum recorded in CD_3OD displays a broad multiplet between 2.69 and 2.36 ppm for the crown thioether protons and a singlet at 3.92 ppm for the methylene protons adjacent to the pyridine moiety. The mass spectrum does not show the molecular peak, but a signal for the fragment $[AuTl(C_6F_5)L(NCMe)]^+$, which clearly suggests the formation of an heterometallic derivative. Further analytical data provided by mass spectroscopy are in agreement with the proposed formulation for the $Au^{I/III}$ and Tl^I complexes **1–4** as summarised in Table 1.

Crystal structures

Single crystals of **1** and **3**·CH_2Cl_2 suitable for X-ray diffraction analysis were grown by slow diffusion of *n*-hexane into a dichloromethane solution of the microcrystalline compounds. Crystals of **4** were grown by slow diffusion of *n*-hexane into a toluene solution of the compound.

In [Tl(L)](PF_6) (**1**), the ligand interacts with the thallium(I) ion through all its donor atoms, imposing a [NS_3] coordination sphere at the metal centre and adopting the typical folded conformation of coordinated pyridine-based 12-membered macrocycles (Fig. 1).[37–41] However, in this case the ligand is not able to fully accommodate the metal ion into its cavity, so that Tl^I is "perching" rather than "nesting" within it, probably because of the dimensions of the metal ion and the presence of a stereochemically active $6s^2$ lone pair (LP). The Tl1–S1 bond distance [3.2030(20) Å] is significantly longer than the other two Tl1–S bond distances [Tl1–S2 3.0032(19) and Tl1–S3 3.0888(17) Å], while the Tl1–N1 bond length is 2.778(5) Å.

In complex **3**·CH_2Cl_2 the ligand **L** adopts a "chair-like" conformation similar to that observed in the solid state for the free ligand:[43] the aliphatic chain of the ring is tilted over the plane containing the pyridine unit as a consequence of the repulsion between the two sulfur atoms close to the aromatic ring.[44] The three S-donors adopt exodentate orientations with the LPs of electrons pointing out of the ring cavity.

The two S-donors close to the pyridine ring are each coordinated to an Au(C_6F_5) moiety (Fig. 2). The two gold(I) centres present an almost linear geometry [C1–Au1–S1 = 175.56(16), C11–Au2–S3 = 177.70(16)°] with Au–S bond distances [2.3131(13), 2.3134(14) Å] in good agreement with those reported in the literature.[45] In the crystal lattice, Au···Au intermolecular interactions of 3.393 Å between neighbouring complex units stabilised by π···π interactions of 3.613 Å between the corresponding slightly offset pentafluorophenyl rings determine the formation of polymeric chains running along the [101] direction (Fig. 3).

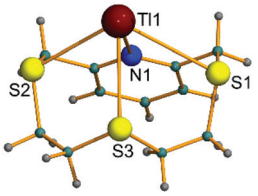

Fig. 1 Molecular structure of complex **1** determined by single crystal X-ray diffraction. Selected bond lengths [Å] and angles [°]: Tl1–N1 2.778(5), Tl1–S1 3.2030(20), Tl1–S2 3.0032(19), Tl1–S3 3.0888(17); N1–Tl1–S2 66.37(12), N1–Tl1–S3 79.98(12), S2–Tl1–S3 68.77(5).

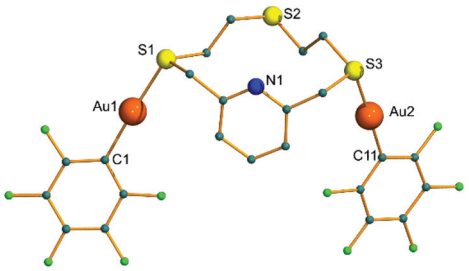

Fig. 2 Molecular structure of complex **3** in **3**·CH_2Cl_2. Selected bond lengths [Å] and angles [°]: Au1–C1 2.027(5), Au1–S1 2.3131(13), Au2–C11 2.028(5), Au2–S3 2.3134(14); C1–Au1–S1 175.56(16), C11–Au2–S3 177.70(16).

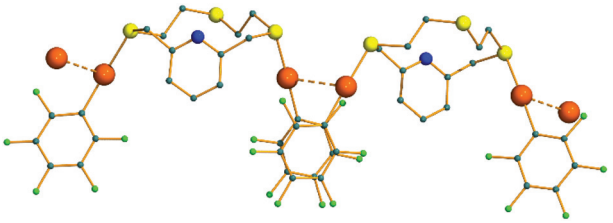

Fig. 3 Association of molecules of **3** in the crystal through aurophilic and π···π interactions forming a chain polymer.

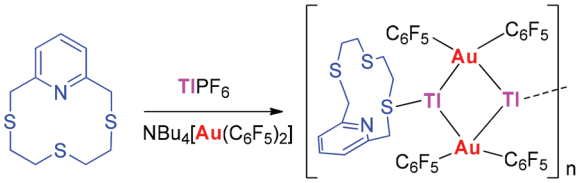

Scheme 2 Synthesis of heterometallic Au^I/Tl^I species **4**.

Open Access Article. Published on 15 June 2021. Downloaded on 1/21/2026 2:17:31 AM.
This article is licensed under a Creative Commons Attribution-NonCommercial 3.0 Unported Licence.

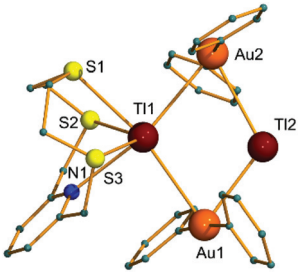

Fig. 4 Molecular structure of complex **4** determined by single crystal X-ray diffraction. Selected bond lengths [Å] and angles [°]: Au1–C1 2.045(4), Au1–C11 2.051(4), Au2–C31 2.047(4), Au2–C41 2.047(4), Au1–Tl2 3.0363(2), Au1–Tl1 3.3660(2), Au2–C31 2.047(4), Au2–C41 2.047(4), Au2–Tl2 3.3505(2), Au2–Tl1 3.3917(2), Au2#–Tl2 3.0299(2), Tl1–N1 2.821(3), Tl1–S3 2.9981(10), Tl1–S1 3.0266(10), Tl1–S2 3.0787(10), Tl1–Tl2 3.7251(2); C1–Au1–C11 174.10(16), Tl2–Au1–Tl1 70.947(5), C31–Au2–C41 177.92(15), Au1–Tl1–Au2 106.323(5), Au2–Tl2–Tl1 56.990(4); # $\frac{1}{2} - x, -\frac{1}{2} + y, \frac{1}{2} - z$.

The crystal structure of compound **4**, collected at 173 K, shows a polymeric Au^I/Tl^I heterodinuclear complex held together by unsupported Au···Tl metallophilic interactions, and composed of a $[Tl(L)]^+$ complex cation, two $[Au(C_6F_5)_2]^-$ anions and a bridging Tl^I metal ion.

The two $[Au(C_6F_5)_2]^-$ aurate units are bridged by two thallium(I) ions to form a neutral tetranuclear assembly with a central cyclic, pseudo-rhombic planar Au_2Tl_2 core *via* Au–Tl interactions ranging from 3.0363(2) to 3.3917(2) Å (Fig. 4). One thallium(I) center (Tl1 in Fig. 4) is also coordinated by the ligand **L** in a similar fashion to that observed in the structure of **1**, while the other thallium(I) ion (Tl2 in Fig. 4) also interacts with the Au(2) center of an adjacent tetranuclear unit, giving rise to zig-zag polymeric chains of neutral $[Au(C_6F_5)_2Tl]_2$ units held together by metallophilic interactions of 3.0299(2) Å, and running along the [010] direction (Fig. 5).

Therefore, the two thallium(I) centres present different coordination environments. Tl1 features and overall NS_3Au_2 hexacoordination resulting from the four macrocycle donor atoms Tl1–N1 2.821(3), Tl1–S1, 3.0266(10), Tl1–S2, 3.0787(10), Tl1–S3 2.9981(10) (Å) and two non-equivalent gold(I) atoms (Au1 and Au2, Fig. 4). Tl2 is characterised by a distorted trigonal planar coordination environment resulting from three gold(I) centres. The gold(I) centres are almost linearly coordinated by the two pentafluorophenyl groups (C–Au–C 174.10(16) and 177.92(15)° for Au1 and Au2, respectively) which lie on different planes, displaying normal Au–C lengths ranging between 2.045(4) and 2.051(4) Å. The two gold(I) centres present a different number of metallophilic interactions with thallium(I) atoms: 2 and 3 for Au1 and Au2, respectively (Fig. 4), resulting in an overall tetra- and pentacoordinated environment, respectively (Fig. 5). The formation of a central planar pseudo-rhombic Au_2Tl_2 core has already been observed for the complex $[\{Au(C_6F_5)_2\}Tl([12]aneNS_3)]_2$ ([12]aneNS$_3$ = 1-aza-4,7,10-trithiacyclododecane).[29] However, in this complex both thallium(I) centres are coordinated by the [12]aneNS$_3$ macrocyclic ligand and the tetranuclear neutral units do not interact each other to form polymeric assemblies, which remains a distinctive structural feature of **4**. Indeed, a discrete nature was also observed for the tetranuclear complexes $[Au_2Tl_2(C_6Cl_5)_4]\cdot(Me_2CO)$,[46] $[Au_2Tl_2(C_6Cl_5)_4](PhMeC{=}O)$, $[Au_2Tl_2(C_6Cl_5)_4](acacH)$ or $[Au_2Tl_2(C_6Cl_5)_4(bipy)](acacH)$[47] which display a butterfly folded Au_2Tl_2 core with intramolecular $Tl^I\cdots Tl^I$ contacts.

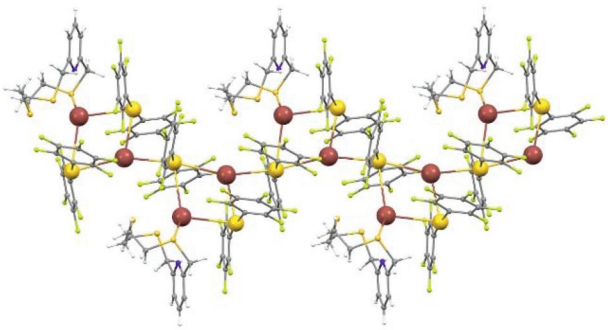

Fig. 5 Zig-zag chain formed by association of tetranuclear Au_2Tl_2 units in **4** through short Au–Tl bonds.

Optical properties

UV-visible diffuse reflectance spectra of the ligand and complexes were performed in the solid state at room temperature. **L** showed an intense band at 280 nm that could be assigned to $\pi \rightarrow \pi^*$ transitions as well as a shoulder at 215 nm that might be due to $n \rightarrow \sigma^*$ transitions within the S–C bonds. All complexes displayed an intense band around 280 nm which, by comparison with the ligand absorption profile, suggests the same origin, *i.e.* IL ($\pi \rightarrow \pi^*$) transitions within the pyridine fragment. Moreover, **3** and **4** show shoulders at *ca.* 252 nm and 240 nm respectively, that could be assigned to $\pi \rightarrow \pi^*$ transitions within the pentafluorophenyl rings.[48] Additionally, these species as well as complex **2** present a broad band at around 350 nm whose tail reaches almost 500 nm. Such low energetic bands could be related to the presence of metal–metal interaction and therefore to MM′CT metal centred transitions involving different metal centres.

Additional photophysical studies were performed in the solid state at 298 K and 77 K. Table 2 summarises the excitation and emission maxima for complexes **3** and **4**, as species **1** and **2** did not show any luminescence under these conditions.

Compound **3** did not display any emission at room temperature. However, when the measurements were performed at 77 K, an emission band centred at 460 nm was observed,

Table 2 Photophysical properties of complexes **3** and **4**

	λ_{em} (λ_{ex})/nm (298 K)	τ/μs (298 K)	λ_{em} (λ_{ex})/nm (77 K)	τ/μs (77 K)
3	—		460 (370)	
4	498 (429)	0.36	510 (<390)	36.5
			478[a], 536 (390–445)	25.3
			550–587 (>450)	16.1

[a] The most intense band.

 This journal is © The Royal Society of Chemistry 2021

Open Access Article. Published on 15 June 2021. Downloaded on 1/21/2026 2:17:31 AM.
This article is licensed under a Creative Commons Attribution-NonCommercial 3.0 Unported Licence.

which might be assigned to a MMCT transitions involving different gold(I) centres based on the presence of intermolecular aurophilic interactions in the solid state (Fig. S5 in the ESI†).

On the contrary, at room temperature, the emission spectrum of complex **4** featured a single band centred at 498 nm when the sample was excited at any wavelength between 300 and 450 nm (Fig. 6). This emission could be assigned to a MM′CT transition involving the gold and thallium centres, as corroborated by the theoretical calculations performed (see below).

By contrast, at 77 K complex **4** displayed three different emissions profiles associated with different excitation spectra (Fig. 7), two of them being red shifted in comparison with the emission at 298 K.

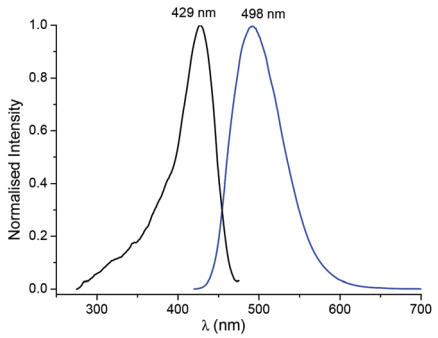

Fig. 6 Excitation (black line) and emission (blue line) spectra for complex **4** at room temperature.

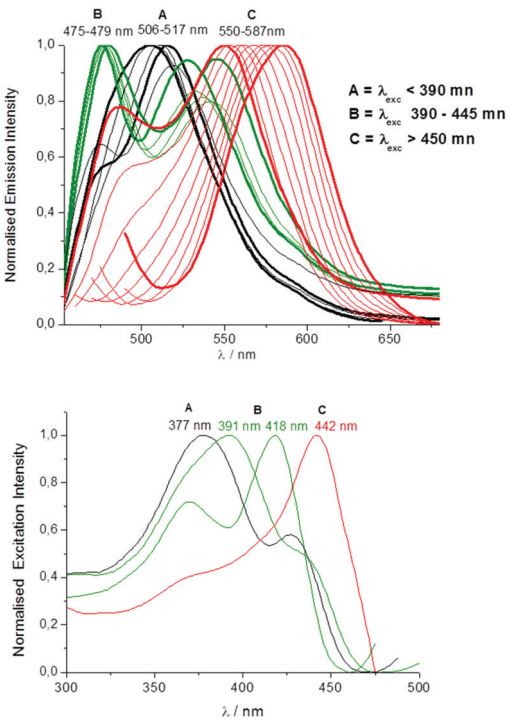

Fig. 7 Normalised emission (top) and their correspondent excitation (bottom) spectra of **4** at 77 K.

Generally, this kind of thermochromic red-shift is associated with the thermal contraction of Au–Tl distances, which promotes an increase in the overlap between Au^I and Tl^I orbitals. A higher orbital overlap reduces the HOMO–LUMO gap, thus lowering the energy of the corresponding emission band.[25] As commented previously, in this particular case there are three different emissions depending on the excitation wavelength. Thus, exciting the sample at wavelengths below 390 nm results in an emission band with maximum intensity at *ca.* 510 nm (black profile, Fig. 7). However, the emission maximum is shifted to *ca.* 570 nm when the excitation was performed at λ_{exc} longer than 450 nm (red profile, Fig. 7). The range of excitation between 390 and 445 nm affords two emission bands, one of them lying as expected between 510 and 570 nm at *ca.* 530 nm, and a second band at higher energy at 478 nm (green profile, Fig. 7 and Table 2).

The overall maxima intensity emission band is centred at 572 nm (Fig. S6 in the ESI†), and is associated with an excitation spectra profile resembling that observed at room temperature (see excitation spectra of Fig. 6 and 7). Therefore, this emission could be considered to have a similar MM′CT origin involving the electron rich $[Au(C_6F_5)_2]$ units and the thallium(I) atoms. In fact, all three emissions and excitation profiles observed at 77 K might have the same origin, considering from one side, that different coordination modes of thallium(I) are present and, from the other side, that the luminescence properties of this type of heterometallic species are mainly affected by differences in the environment of thallium(I) atoms.[49,50] In this case, complex **4** presents two thallium(I) atoms with different coordination modes, distorted hexacoordinated and trigonal planar, respectively. Tl–Au distances at 173 K varies from 3.03 to 3.39 Å and at 77 K may be remarkably different, shorter than those at higher temperature, thus rendering lower the energy gap among the excited states and different orbital overlapping. In particular, the geometry contraction at such temperature might promote different emission and excitation patterns from each thallium environment. The assignment of those profiles to a specific Tl environment is complex. However, by comparison with previous reports,[50,51] it can be suggested that emission at lower energies might be due to the Tl^I atom in a distorted trigonal planar environment, whereas emissions at higher energies might come from the hexacoordinated thallium(I) centre. In addition, lifetimes of complex **4** were measured for all the emission bands observed at 77 K and at 298 K. As expected, the excited state lifetime value increases from 0.36 μs to 36.5 μs when lowering the temperature to 77 K. The microsecond range of the lifetime indicates the phosphorescence nature of the emission.

DFT calculations

Theoretical calculations represent an invaluable tool in investigating systems as different as optical materials,[52] redox-active compounds,[53,54] or weakly bonded solid-state assemblies. In this context, DFT calculations[55] have been largely adopted to investigate weak interactions such as hydrogen, halogen or chalcogen bonding and metal–metal interactions, and at the

Open Access Article. Published on 15 June 2021. Downloaded on 1/21/2026 2:17:31 AM.
This article is licensed under a Creative Commons Attribution-NonCommercial 3.0 Unported Licence.

same time solid-state absorption and emission properties.[56] We have, therefore, turned to investigate the absorption and emission features of compound **4** by means of computational studies in order to rationalize the optical properties observed experimentally on the base of its structural features. Due to the polymeric nature of compound **4**, in order to take into account all the metallophilic interactions present in the compound and to represent the different coordination environments for each Au^I and Tl^I center, the oligomeric portion $\{LTl_2[Au(C_6F_5)_2]_2\}_3$ (**4′**), composed of 234 atoms, has been selected to investigate the electronic structure of **4** in the solid state (Fig. S7†), by keeping an adequate balance with the computational cost to perform DFT and TD-DFT calculations (see Tables S1 and S2†). DFT calculations were carried out with the mPW1PW hybrid functional[57] successfully adopted in the case of different, albeit monomeric, gold complexes featuring potential-controlled emission energies.[58] All calculations were carried out at the frozen geometry extracted from structural data collected at 173(2) K. An analysis of the Kohn–Sham molecular orbitals (MOs) calculated for compound **4′** shows that MOs can be grouped as follows (see Fig. S8† for selected MOs drawings):

(a) The HOMO (MO #810) is centred exclusively on gold atoms;

(b) HOMO−1 and HOMO−2 (MO #809 and #808) are non-bonding orbitals centred on both gold and thallium atoms;

(c) More inner orbitals (#796 to 807) are MOs located on $[Au(C_5F_5)]_2^-$ anions, with a large contribution from the π-aromatic system of the perfluorophenyl ligands.

(d) The LUMO (MO #811) and its immediately higher virtual MOs are mainly centred on the thallium atoms.

Although calculations are limited to a small portion of the polymeric structure, it can be deduced that they reflect the electronic structure of the compound. A natural population analysis[59] shows that the charge on the thallium atoms is remarkably dependent on their coordination environment, with the charge on the planar coordinated thallium atom Tl2, only surrounded by gold atoms, being sensibly larger (+0.944 $|e|$) than that on the hexacoordinated Tl1 (+0.586 $|e|$), which is lowered by the electron donation from the macrocycle S-donor atoms.

In order to investigate the absorption and emission properties of **4**, the absorption spectrum was simulated for **4′** (Fig. 8) based on the pattern of transitions evaluated at the time-dependent DFT (TD-DFT) level of theory (Table 3 and Fig. 9).

The simulated spectrum (Fig. 8) results from two main groups of transitions (Table 3 and Fig. 9). The singlet S0 → S1 and S0 → S2 vertical transitions are responsible for an absorption centred at about 400 nm. These transitions arise from monoelectronic excitations from the HOMO and HOMO−1, respectively, to the LUMO. Therefore, both transitions have a metal-to-metal Charge Transfer (MM′CT) character. The transitions from the ground state S0 to the excited states S3 to S7 are all forbidden, with negligible oscillator strength values. The most intense transitions ($f > 0.10$) are S0 → S8 and S0 → S9, falling at about 3.7 eV. Both involve excitations from inner MOs (HOMO−2 and HOMO−9, respectively), featuring a large

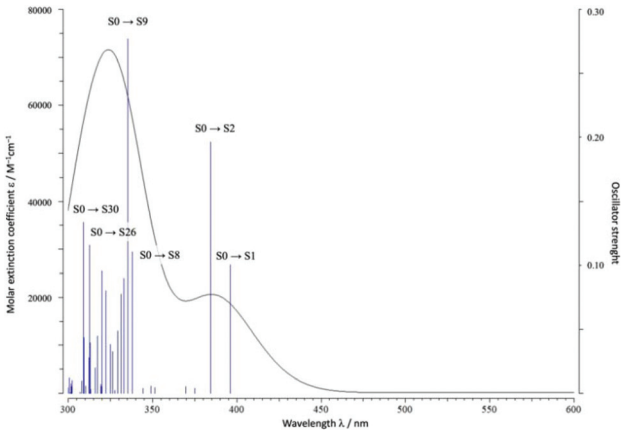

Fig. 8 Simulated UV-vis absorption spectrum at TD-DFT level based on singlet–singlet excitations calculated for the model system $\{LTl_2[Au(C_6F_5)_2]_2\}_3$ (**4′**).

Table 3 Wavelengths (λ_{calc}, nm), energy (E, eV), oscillator strength (f), and monoelectronic excitation contributions of the main vertical transitions ($f > 0.10$) calculated for **4′** at TD-DFT level

Exc. state	λ_{calc}	E	f	Main MO contribution
S1	396.3	3.128	0.100	HOMO → LUMO
				HOMO−1 → LUMO
S2	384.7	3.222	0.196	HOMO−1 → LUMO
				HOMO−2 → LUMO
S8	338.0	3.669	0.109	HOMO−2 → LUMO+3
S9	335.6	3.695	0.281	HOMO−9 → LUMO
				HOMO−5 → LUMO
				HOMO−3 → LUMO
S26	312.7	3.965	0.127	HOMO → LUMO+8
				HOMO → LUMO+4
				HOMO−2 → LUMO+5
S30	309.0	4.013	0.144	HOMO−14 → LUMO
				HOMO−1 → LUMO+8
				HOMO−1 → LUMO+15

contribution from gold species and from perfluorophenyl ligands, to LUMO+3 and LUMO, respectively, localized on Tl^I atoms. Therefore, this group of transitions can be considered MM′CT and LMCT in nature. Intense transitions at about 4 eV are calculated to have the same character.

The presence of two main groups of absorption bands in the region 300–500 nm is in agreement with the excitation spectra experimentally recorded for **4** (Fig. 7), and allows to hypothesise the nature of the emission spectra:

(1) At room temperature (RT) excitation at 429 nm (Fig. 6) results in the S0 → S1 and S0 → S2 electron transitions, which are followed by a LUMO → HOMO (Tl → Au CT) radiative relaxation corresponding to the phosphorescent emission at about 500 nm (Table 2). The lowering of the temperature down to 77 K is likely to shorten the intermetallic Au···Tl and hence to reduce the HOMO–LUMO energy gap, reflected in the emission at 550–590 nm (Table 2) upon excitation at $\lambda_{exc} > 450$ nm at 77 K.

(2) When the absorption occurs at higher energy, excitation to higher excited states (≥S8) is achieved. At room temperature the overlap of the vibrational manifolds allows for an internal

 This journal is © The Royal Society of Chemistry 2021

Open Access Article. Published on 15 June 2021. Downloaded on 1/21/2026 2:17:31 AM.
This article is licensed under a Creative Commons Attribution-NonCommercial 3.0 Unported Licence.

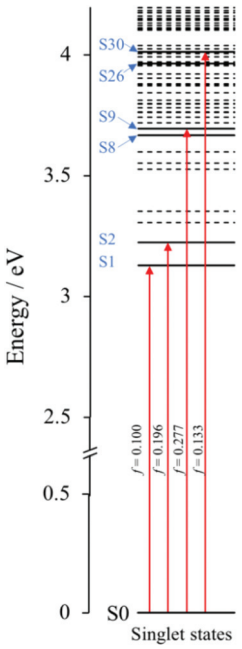

Fig. 9 Singlet excited state diagram (0.0–4.2 eV) calculated for the model system $\{LTl_2[Au(C_6F_5)_2]_2\}_3$ (**4′**) at the TD-DFT level (see Table 3). The excited states with transitions from the ground state featuring negligible oscillator strengths ($f \leq 0.10$) are represented as dotted lines.

conversion (IC) to the lowest excited state S1 followed by radiative relaxation to the GS S0. This hypothesis is in agreement with the fact that at RT a single emission at about 500 nm is observed whatever the excitation wavelength used in the range 300–450 nm.

(3) At 77 K, structural variations (see above) as well as a different extent of overlap between MOs belonging to the differently coordinated Tl ions and the gold atoms might allow to discriminate between Tl(1) → Au and Tl(2) → Au relaxations, thus accounting for the dual luminescence observed only at 77 K. The values of the relaxation times τ (Table 2) suggest a role of intersystem crossing (ISC) from singlet to triplet states mediated by spin–orbit coupling, followed by a triplet radiative emission, in agreement with experimental measurements.

Experimental section

Experimental details

^{1}H, ^{13}C{^{1}H}, and ^{19}F{^{1}H} NMR were recorded at room temperature on a BRUKER AVANCE 400 spectrometer (^{1}H, 400 MHz; ^{13}C, 100.6 MHz; ^{19}F, 377 MHz) with chemical shifts (δ, ppm) and reported relative to the solvent peaks of the deuterated solvent. Mass spectra were recorded on a BRUKER ESQUIRE 3000 PLUS, with the electrospray (ESI) technique and on a BRUKER MICROFLEX (MALDI-TOF), with a Ditranol or a T-2-(3-(4-*t*Butyl-phenyl)-2-methyl-2 propenylidene)malononitrile matrix. UV/vis spectra were recorded with Jasco V-670 spectrophotometer fitted with a Praying Mantis diffuse reflectance accessory. Room temperature steady-state emission and excitation spectra were recorded with a Jobin–Yvon–Horiba fluorolog FL3-11 spectrometer. Infrared spectra were measured in the range 4000–250 cm^{-1} on a PerkinElmer Spectrum 100 FTIR spectrometer as KBr pellets.

Crystal structure determinations

Crystals were mounted in inert oil on glass fibres and transferred to the cold gas stream of an Xcalibur Oxford Diffraction diffractometer equipped with a low-temperature attachment. Data were collected using monochromated MoKα radiation (λ = 0.71073 Å). Scan type ϖ. Absorption corrections based on multiple scans were applied using spherical harmonics implemented in SCALE3 ABSPACK scaling algorithm.[60] The structures were solved by direct methods and refined on F^2 using the program SHELXT-2016.[61] All non-hydrogen atoms were refined anisotropically. CCDC deposition numbers 2083080 (**1**), 2083081 (**3**) and 2083082 (**4**)† contain the supplementary crystallographic data.

Materials and procedures

$TlPF_6$ and $AuCl_3{\cdot}nH_2O$ and solvents were purchased from commercial suppliers and used as received unless otherwise stated. $[Au(C_6F_5)(tht)]$,[62] $[Au(C_6F_5)_2]NBu_4$[63] and **L**[42] were prepared according to literature procedures.

Synthesis of the complexes 1–4

Synthesis of [Tl(L)]PF$_6$ (1). $TlPF_6$ (74.2 mg, 0.210 mmol) was added to a solution of **L** (72.4 mg, 0.210 mmol) in CH_2Cl_2 (10 mL). The mixture was stirred at room temperature for 2 h. A white solid was obtained by evaporation of the solvent under reduced pressure. Then, the solid was washed with diethyl ether (125.3 mg, 97% yield). White crystals were obtained by slow diffusion of *n*-hexane into a solution of the complex in CH_2Cl_2. MS (MALDI$^+$): *m*/*z* 462.0 ([(**L**Tl)$^+$] 100%), calculated 462.0. ^{1}H NMR (400 MHz, CD_2Cl_2): δ_H 7.84 (t, *J* = 7.7 Hz, 1H, C*H*$_p$(Py)), 7.39 (d, *J* = 7.7 Hz, 2H C*H*$_m$(Py)), 4.17 (s, 4H, SC*H*$_2$Py), 2.95 (s$_{br}$, 4H, SC*H*$_2$C*H*$_2$S), 2.61 (s$_{br}$, 4H, SC*H*$_2$C*H*$_2$S). ^{13}C NMR (101 MHz, CD_2Cl_2): δ_C 158.97 *C*H$_o$(Py), 139.83 *C*H$_p$(Py), 125.39 *C*H$_m$(Py), 38.10 (*S*CH$_2$Py), 33.25 and 30.95 (*S*CH$_2$*C*H$_2$S). FT-IR (KBr pellet, ν, cm^{-1}), (P–F): 827 (vs).

Synthesis of [AuCl$_3$(L)] (2). A solution of $AuCl_3{\cdot}nH_2O$ (50.0 mg, 0.130 mmol) in acetone (5 mL) was added dropwise to a solution of **L** (32.7 mg, 0.13 mmol) in CH_2Cl_2 (5 mL). The mixture was stirred at room temperature for 1 h and then *n*-hexane (10 mL) was added to force the precipitation of [AuCl$_3$(**L**)]. The precipitate was filtered and washed with further *n*-hexane (15 mL) and diethyl ether (15 mL) to give an orange solid (63.6 mg, 89% yield). MS (MALDI$^+$): *m*/*z*, 454.2 [(M − 3Cl)$^+$] calculated 454.2, ^{1}H NMR (400 MHz, $(CD_3)_2CO$): δ_H 8.76 (t, *J* = 8.0 Hz, 1H, C*H*$_p$(Py)), 8.22 (d, *J* = 8.0 Hz, 2H, C*H*$_m$(Py)), 4.59 (s, 4H, SC*H*$_2$Py), 2.85 (s$_{br}$, 4H, SC*H*$_2$C*H*$_2$S), 2.75 (s$_{br}$, 4H, SC*H*$_2$C*H*$_2$S). ^{13}C NMR (101 MHz, $(CD_3)_2CO$): δ_C 154.86 *C*H$_o$(Py), 148.77 *C*H$_p$(Py), 127.83 *C*H$_m$(Py), 31.76 (*S*CH$_2$Py), 31.02 (*S*CH$_2$*C*H$_2$S), FT-IR (KBr pellet, ν, cm^{-1}), (Au–Cl): 333 (vs). Note: the ^{13}C NMR signal of one of the carbons (–*S*CH$_2$*C*H$_2$S–) is hidden under septuplet peak of the solvent.

Open Access Article. Published on 15 June 2021. Downloaded on 1/21/2026 2:17:31 AM.
This article is licensed under a Creative Commons Attribution-NonCommercial 3.0 Unported Licence.

Synthesis of [{Au(C_6F_5)}$_2$(μ-L)] (3). A solution of [Au(C_6F_5)(tht)] (97.6 mg, 0.220 mmol) in CH_2Cl_2 (5 mL) was added dropwise to a solution of **L** (27.8 mg, 0.11 mmol) in CH_2Cl_2 (5 mL). The mixture was stirred at room temperature for 2 hours and then, *n*-hexane (10 mL) was added. Evaporation of CH_2Cl_2 under reduced pressure afforded a white solid. The precipitate was filtered and washed with *n*-hexane (15 mL) (54.6 mg, 50% yield). White crystals were obtained by slow diffusion of *n*-hexane into a solution of the complex in CH_2Cl_2. MS (MALDI$^+$): *m*/*z* 817.9 [(M − C_6F_5)$^+$] calculated 817.9, 622.0 [(M − (C_6F_5)Au + H)$^+$] calculated 622.0, 454.0 [(M − (C_6F_5)$_2$Au)$^+$] calculated 454.0. ^{1}H NMR (400 MHz, CD_2Cl_2): δ_H 8.01–7.91 (m, 1H, C*H*$_p$(Py)), 7.85–7.75 (m, 2H, C*H*$_m$(Py)), 4.55 (s$_{br}$, 1H, SC*H*$_2$Py), 4.39 (s$_{br}$, 2H, SC*H*$_2$Py), 4.05 (s$_{br}$, 1H, SC*H*$_2$Py), 3.69 (s$_{br}$, 2H, SC*H*$_2$C*H*$_2$S), 3.25 (s$_{br}$, 4H, SC*H*$_2$C*H*$_2$S), 2.95 (s$_{br}$, 2H, SC*H*$_2$C*H*$_2$S). ^{19}F NMR (377 MHz, $(CD_3)_2CO$): δ_F −117.93 (m, F$_{orto}$), −162.13 (t, *J* = 19.9 Hz, F$_{para}$), −165.49 (t, *J* = 19.7 Hz, F$_{meta}$). FT-IR (KBr disk, ν, cm^{-1}), (C–F): 1504 (vs), 954 (vs), 798(s) (P–F): 826 (vs).

Synthesis of {[Au(C_6F_5)$_2$Tl]$_2$(L)}$_n$ (4). A mixture of **L** (50.1 mg, 0.190 mmol), $TlPF_6$ (126 mg, 0.380 mmol) and [Au(C_6F_5)$_2$]NBu_4 (294 mg, 0.380 mmol) in CH_2Cl_2 (20 mL) was stirred at room temperature for 2 h. *n*-Hexane (15 mL) was added to the reaction mixture and a light green solid precipitated. The filtered solid was washed with CH_2Cl_2. MS (MALDI$^+$): *m*/*z* 462.0 ([(**L**Tl)$^+$] 100%), calculated 462.0; 867.6 ([(M − TlAu(C_6F_5)$_3$ + CH_3CN)$^+$] 2.6%), calculated 867.0. ^{1}H NMR (400 MHz, CD_3OD): δ_H 7.83 (t, *J* = 7.7 Hz, 1H), 7.43 (d, *J* = 7.7 Hz, 2H), 3.92 (s, 4H), 2.69–2.36 (m, 8H). ^{13}C NMR (101 MHz, CD_3OD): δ_C 159.20 C*H*$_o$(Py), 150.0 (m, *o*-C_6F_6), 139.92 C*H*$_p$(Py), 138.9 (m, *p*-C_6F_6), 138.1 (m, *m*-C_6F_6), 123.77 C*H*$_m$(Py), 36.97, (S*C*H$_2$Py), 32.12, 31.04 (S*C*H$_2$*C*H$_2$S^{19}F NMR (377 MHz, CD_3OD): δ_F −74.6 (d, J_{F-P} = 709, PF_6), −75.52 (s, PF_6), from −116.75 to −116.96 (m, F$_{orto}$), from −164.92 to −165.12 (m, F$_{para}$), from −166.07 to −166.42 (m F$_{meta}$). FT-IR (KBr disk, ν, cm^{-1}), (C–F): 1506 (vs), 943 (vs), 786(s), (P–F): 826 (vs).

Theoretical calculations

Quantum-chemical calculations were carried out on the fragment **4′**, {LTl$_2$[Au(C_6F_5)$_2$]$_2$}$_3$, at DFT level with the commercial suite of computational software Gaussian 16.[64] The mPW1PW functional[55] was paralleled by the full-electron double-ζ basis sets[65–68] for light atomic species and the SBKJC BS with relativistic effective core potentials (RECPs) for gold and thallium. The atomic coordinates of each atomic species were extracted from the structural data and not optimised. Both the electronic structure corresponding to the singlet and triplet ground states (GSs; S0 and T0, respectively) were calculated. A complete natural population analysis (NPA) was carried out with a Natural Bonding Orbital (NBO)[59] partitioning scheme in order to investigate the charge distributions. Absorption transitions energies *E*, wavelengths λ_{calc}, oscillator strengths *f* were calculated at the TD-DFT level of theory (50 singlet states). GaussView 6.0[69] was used to analyse the charge distribution, MOs isosurfaces and simulated absorption spectra.

Conclusions

The coordination behaviour of the macrocyclic ligand 2,5,8-trithia[9](2,6)pyridinophane (**L**) towards thallium(I), gold(III) and gold(I) has been investigated. The coordination of **L** to the thallium(I) centre in the ionic complex [Tl(L)](PF_6) (**1**) takes places through all the sulfur and nitrogen donor atoms, in a distorted square-pyramidal geometry with the thallium atom in the apical position and with the presence of the inert LP of electrons. Gold(III) is bonded by the ligand in [AuCl$_3$(L)] (**2**) only through the nitrogen of the pyridine group, whereas the coordination of one Au^I–C_6F_5 fragment to each of the sulfur atoms of the ligand next to the pyridine moiety occurs in [{Au(C_6F_5)}$_2$(μ-L)] (**3**). The presence of secondary interactions such as aurophilic interactions and π···π contacts between pentafluorophenyl rings originates a linear polymer. The heterometallic Tl^I/Au^I polymeric complex {[Au(C_6F_5)$_2$Tl]$_2$(L)}$_n$ (**4**) features a metallic pseudo-rhombic planar Au_2Tl_2 core that repeats itself to form zig-zag polymers. In each Au_2Tl_2 moiety only one of the thallium atoms exhibits a pseudo-octahedral geometry, bonded to the NS_3 donor set of the macrocyclic ligand and forming two additional unsupported Au–Tl bonds with two [Au(C_6F_5)$_2$]$^-$ units. The other thallium atom is the nexus with the neighbouring Au_2Tl_2 unit, and exhibits a distorted trigonal planar geometry, being bonded only with three gold atoms with unsupported Au–Tl interactions. This complex displays an interesting thermochromic behaviour showing emissions that were assigned to MM′CT metal centred transitions at room temperature, whereas at 77 K it shows a dual emission probably coming from the two different thallium environments. A natural population analysis carried out at DFT level confirms the different nature of the two Tl centres, the trigonally coordinated one showing the most positive charge. TD-DFT calculations allowed to evaluate the nature of the absorption singlet transitions in the UV-vis region and therefore, the excitation path, and corroborate the hypothesis that the origin of the low energy emissions can be considered MM′CT Tl → Au in nature with a partial contribution from (Tl → C_6F_5Au) MLCT transitions. The nature of the transitions suggests that small structural changes occurring on changing the temperature may largely affect the degree of overlap between the MOs involved in the gold(I)–thallium(I) interactions, thus modifying the relaxation pathways and therefore accounting for the thermochromism observed experimentally.

Conflicts of interest

There are no conflicts to declare.

Acknowledgements

Authors thank the Agencia Estatal de Investigación (projects PID2019-104379RB-C21, RTI2018-097836-J100 and RYC2018-025872), Gobierno de Aragón–Fondo Social Europeo (Research

 This journal is © The Royal Society of Chemistry 2021

Open Access Article. Published on 15 June 2021. Downloaded on 1/21/2026 2:17:31 AM.
This article is licensed under a Creative Commons Attribution-NonCommercial 3.0 Unported Licence.

Group E07_20R) and the Fondazione di Sardegna (FdS) and Regione Autonoma della Sardegna (RAS) (Progetti Biennali di Ateneo FdS/RAS annualità 2018) for financial support of our research. A. P. acknowledges RAS for the funding in the context of the POR FSE 2014–2020 (CUP F24J17000190009).

Notes and references

1 H. Schmidbaur and A. Schier, *Chem. Soc. Rev.*, 2008, **37**, 1931–1951; H. Schmidbaur and A. Schier, *Chem. Soc. Rev.*, 2012, **41**, 370–412.
2 E. J. Fernández, A. Laguna, J. M. López-de-Luzuriaga, M. Monge, M. Montiel, M. E. Olmos and M. Rodríguez-Castillo, *Dalton Trans.*, 2009, 7509–7518.
3 M. J. Calhorda, C. Ceamanos, O. Crespo, M. C. Gimeno, A. Laguna, C. Larraz, P. D. Vaz and M. D. Villacampa, *Inorg. Chem.*, 2010, **49**, 8255–8269.
4 O. Crespo, M. C. Gimeno, A. Laguna, F. J. Lahoz and C. Larraz, *Inorg. Chem.*, 2011, **50**, 9533–9544.
5 D. Rios, M. M. Olmstead and A. L. Balch, *Inorg. Chem.*, 2009, **48**, 5279–5287.
6 M. C. Blanco, J. Cámara, M. C. Gimeno, A. Laguna, S. L. James, M. C. Lagunas and M. D. Villacampa, *Angew. Chem., Int. Ed.*, 2012, **51**, 9777–9779.
7 L. Gade, *Angew. Chem., Int. Ed.*, 2001, **40**, 3573–3575.
8 R. Echeverría, J. M. López-de-Luzuriaga, M. Monge and M. E. Olmos, *Chem. Sci.*, 2015, **6**, 2022–2026.
9 J. M. López-de-Luzuriaga, M. Monge, M. E. Olmos and D. Pascual, *Inorg. Chem.*, 2014, **53**, 1275–1277.
10 J. M. López-de-Luzuriaga, M. Monge, S. Moreno, M. E. Olmos and M. Rodríguez-Castillo, *Angew. Chem.*, 2021, **60**, 640–644.
11 P. Pyykkö, *Chem. Rev.*, 1997, **97**, 597–636.
12 P. Pyykkö, *Chem. Soc. Rev.*, 2008, **37**, 1967–1997.
13 A. J. Blake, R. Donamaría, V. Lippolis, J. M. Lopez-de-Luzuriaga, M. Monge, M. E. Olmos, A. Seal and J. A. Weinstein, *Inorg. Chem.*, 2019, **58**, 4954–4961.
14 *Modern Supramolecular Gold Chemistry: Gold-Metal Interactions and Applications*, ed. A. Laguna, Wiley-VCH, Weinheim, Germany, 2008, ISBN: 978-352732095.
15 J. M. Forward, J. P. Fackler Jr. and Z. Assefa, Optoelectronic Properties of Inorganic Compounds, in *Photophysical and Photochemical Properties of Gold(I) Complexes*, ed. D. M. Roundhill and J. P. Fackler Jr., Springer, US, 1999, ISBN: 978-1475761016.
16 V. W.-W. Yam, V. K.-M. Au and S. Y.-L. Leung, *Chem. Rev.*, 2015, **115**, 7589–7728.
17 M. J. Katz, K. Sakai and D. B. Leznoff, *Chem. Soc. Rev.*, 2008, **37**, 1884–1895.
18 X. Zhang, B. Li, Z.-H. Chen and Z.-N. Chen, *J. Mater. Chem.*, 2012, **22**, 11427–11441.
19 C. E. Strasser and V. J. Catalano, *J. Am. Chem. Soc.*, 2010, **132**, 10009–10011.
20 R. Visbal and M. C. Gimeno, *Chem. Soc. Rev.*, 2014, **43**, 3551–3574.
21 E. J. Fernández, A. Laguna and J. M. López-de-Luzuriaga, *Dalton Trans.*, 2007, 1969–1981.
22 J. M. López-de-Luzuriaga, M. Monge and M. E. Olmos, *Dalton Trans.*, 2017, **46**, 2046–2067.
23 R. J. Roberts, D. Le and D. B. Leznoff, *Chem. Commun.*, 2015, **51**, 14299–14302.
24 S. H. Lim, M. M. Olmstead and A. L. Balch, *J. Am. Chem. Soc.*, 2011, **133**, 10229–10238.
25 E. J. Fernández, J. M. López-de-Luzuriaga, M. Monge, M. E. Olmos, J. Pérez, A. Laguna, A. A. Mohammed and J. P. Fackler Jr., *J. Am. Chem. Soc.*, 2003, **125**, 2022–2023.
26 R. Donamaria, V. Lippolis, J. M. López-de-Luzuriaga, M. Monge, M. Nieddu and M. E. Elmos, *Dalton Trans.*, 2020, **49**, 10983–10993.
27 A. J. Blake, R. Donamaría, E. J. Fernández, T. Lasanta, V. Lippolis, J. M. Lopez-de-Luzuriaga, E. Manso, M. Monge and M. E. Olmos, *Dalton Trans.*, 2013, **42**, 11559–11570.
28 A. J. Blake, R. Donamaría, V. Lippolis, J. M. Lopez-de-Luzuriaga, E. Manso, M. Monge and M. E. Olmos, *Inorg. Chem.*, 2014, **53**, 10471–10484.
29 R. Donamaría, V. Lippolis, J. M. Lopez-de-Luzuriaga, M. Monge, M. Nieddu and M. E. Olmos, *Inorg. Chem.*, 2017, **56**, 12551–12563.
30 R. Donamaría, V. Lippolis, J. M. Lopez-de-Luzuriaga, M. Monge, M. Nieddu and M. E. Olmos, *Inorg. Chem.*, 2018, **57**, 11099–11112.
31 R. Donamaría, V. Lippolis, J. M. Lopez-de-Luzuriaga, M. Monge, M. Nieddu and M. E. Olmos, *Chem. – Eur. J.*, 2018, **24**, 13740–13743.
32 R. Donamaría, V. Lippolis, J. M. Lopez-de-Luzuriaga, M. Monge, M. Nieddu and M. E. Olmos, *Inorg. Chem.*, 2020, **59**, 6398–6409.
33 A. Bencini and V. Lippolis, *Coord. Chem. Rev.*, 2012, **256**, 149–169.
34 V. Lippolis and M. Shamsipur, *J. Iran. Chem. Soc.*, 2006, **3**, 105–127.
35 L. Lvova, F. Caroleo, A. Garau, V. Lippolis, L. Giorgi, V. Fusi, N. Zaccheroni, M. Lombardo, L. Prodi, C. Di Natale and R. Paolesse, *Front. Chem., Sect. Anal. Chem.*, 2018, **6**, 258 and refs. therein.
36 A. Casula, V. Nairi, V. Fernández-Moreira, A. Laguna, V. Lippolis, A. Garau and M. C. Gimeno, *Dalton Trans.*, 2015, **44**, 18506–18517.
37 A. Garau, G. Picci, M. Arca, A. J. Blake, C. Caltagirone, G. De Filippo, F. Demartin, F. Isaia, V. Lippolis, A. Pintus, M. A. Scorciapino and M. C. Aragoni, *Molecules*, 2021, **26**, 1286.
38 O. K. Rasheed, C. Bawn, D. Davies, J. Raftery, I. Victorica-Yrzebal, R. Pritchard, H. Zhou and P. Quayle, *Eur. J. Inorg. Chem.*, 2017, **35**, 5252–5261.
39 P. J. Reddy, V. Ravichandran and K. K. Chacko, *Acta Crystallogr., Sect. C: Cryst. Struct. Commun.*, 1989, **45**, 1871–1874.
40 M. E. Sobhia, K. Panneerselvam and K. K. Chacko, *Inorg. Chim. Acta*, 1992, **194**, 93–97.

Open Access Article. Published on 15 June 2021. Downloaded on 1/21/2026 2:17:31 AM.
This article is licensed under a Creative Commons Attribution-NonCommercial 3.0 Unported Licence.

41 A. J. Blake, F. Demartin, F. A. Devillanova, A. Garau, F. Isaia, V. Lippolis, M. Schröder and G. Verani, *J. Chem. Soc., Dalton Trans.*, 1996, 3705–3712.
42 M. Arca, A. J. Blaake, J. Casabò, F. Demartin, F. A. Devillanova, A. Garau, F. Isaia, V. Lippolis, R. Kivekas, V. Muns, M. Schröder and G. Verani, *J. Chem. Soc., Dalton Trans.*, 2001, 1180–1188.
43 G. Weber, P. G. Jones and G. M. Sheldrick, *Acta Crystallogr., Sect. C: Cryst. Struct. Commun.*, 1983, **39**, 389–391.
44 J. Casabò, L. Escriche, S. Alegret, C. Jaime, C. Perez-Jimenez, J. Rius, E. Molins, C. Miravitlles, F. Teixidor and L. Mestres, *Inorg. Chem.*, 1991, **30**, 1893–1898.
45 F. Caddeo, V. Fernández Moreira, M. Arca, A. Laguna, V. Lippolis and M. C. Gimeno, *Inorganics*, 2014, **2**, 424–432.
46 E. J. Fernández, J. M. López-de-Luzuriaga, M. Monge, M. E. Olmos, J. Pérez and A. Laguna, *J. Am. Chem. Soc.*, 2002, **124**, 5942–5943.
47 E. J. Fernández, J. M. López-de-Luzuriaga, M. E. Olmos, J. Pérez, A. Laguna and M. C. Lagunas, *Inorg. Chem.*, 2005, **44**, 6012–6018.
48 E. J. Fernández, A. Laguna, J. M. López-de-Luzuriaga, M. Monge, M. Montiel and M. E. Olmos, *Inorg. Chem.*, 2005, **44**, 1163–1165.
49 E. J. Fernández, A. Laguna, J. M. López-de-Luzuriaga, M. Monge and F. Mendizabal, *J. Mol. Struct.: THEOCHEM*, 2008, **851**, 121–126.
50 E. J. Fernández, A. Laguna, J. M. López-de-Luzuriaga, F. Mendizabal, M. Monge, M. E. Olmos and J. Pérez, *Chem. – Eur. J.*, 2003, **9**, 456–465.
51 E. J. Fernández, A. Laguna, J. M. López-de-Luzuriaga, M. E. Olmos and J. Pérez, *Chem. Commun.*, 2003, 1760–1761.
52 M. Nishiwaki and H. Fujiwara, *Comput. Mater. Sci.*, 2020, **172**, 109315.
53 R. Perochon, F. Barriere, O. Jeannin, L. Piekara-Sady and M. Formigué, *Chem. Commun.*, 2021, **57**, 1615–1618.
54 M. C. Aragoni, M. Arca, M. Caironi, C. Denotti, F. A. Devillanova, E. Grigiotti, F. Isaia, F. Laschi, V. Lippolis, D. Natali, L. Pala, M. Sampietro and P. Zanello, *Chem. Commun.*, 2004, 1882–1883.
55 W. Koch and M. C. Holthausen, *A Chemist's Guide to Density Functional Theory*, Wiley–VCH Verlag GmbH, 2nd edn, 2001.
56 S.-C. Qi, J. Hayashi and L. Zhang, *RSC Adv.*, 2016, **6**, 77375–77395.
57 C. Adamo and V. Barone, *J. Chem. Phys.*, 1998, **108**, 664–975.
58 M. C. Aragoni, M. Arca, F. A. Devillanova, F. Isaia, V. Lippolis and A. Pintus, *Chem. – Asian J.*, 2011, **6**, 198–208.
59 A. E. Reed, R. B. Weinstock and F. Weinhold, *J. Chem. Phys.*, 1985, **83**, 735–746.
60 CrysAlisPro, Agilent Technologies, Version 1.171.35.11. Multi-scans absorption correction with SCALE3 ABSPACK scaling algorithm.
61 G. Sheldrick, *Acta Crystallogr., Sect. A: Found. Adv.*, 2015, **71**, 3–8.
62 R. Uson, A. Laguna and J. Vicente, *J. Organomet. Chem.*, 1977, **131**, 471–475.
63 R. Usón, A. Laguna and J. Vicente, *J. Chem. Soc., Chem. Commun.*, 1976, 353–354.
64 M. J. Frisch, G. W. Trucks, H. B. Schlegel, G. E. Scuseria, M. A. Robb, J. R. Cheeseman, G. Scalmani, V. Barone, G. A. Petersson, H. Nakatsuji, X. Li, M. Caricato, A. V. Marenich, J. Bloino, B. G. Janesko, R. Gomperts, B. Mennucci, H. P. Hratchian, J. V. Ortiz, A. F. Izmaylov, J. L. Sonnenberg, D. Williams-Young, F. Ding, F. Lipparini, F. Egidi, J. Goings, B. Peng, A. Petrone, T. Henderson, D. Ranasinghe, V. G. Zakrzewski, J. Gao, N. Rega, G. Zheng, W. Liang, M. Hada, M. Ehara, K. Toyota, R. Fukuda, J. Hasegawa, M. Ishida, T. Nakajima, Y. Honda, O. Kitao, H. Nakai, T. Vreven, K. Throssell, J. A. Montgomery Jr., J. E. Peralta, F. Ogliaro, M. J. Bearpark, J. J. Heyd, E. N. Brothers, K. N. Kudin, V. N. Staroverov, T. A. Keith, R. Kobayashi, J. Normand, K. Raghavachari, A. P. Rendell, J. C. Burant, S. S. Iyengar, J. Tomasi, M. Cossi, J. M. Millam, M. Klene, C. Adamo, R. Cammi, J. W. Ochterski, R. L. Martin, K. Morokuma, O. Farkas, J. B. Foresman and D. J. Fox, *Gaussian 16, Revision B.01*, Gaussian, Inc., Wallingford CT, 2016.
65 A. Schafer, H. Horn and R. Ahlrichs, *J. Chem. Phys.*, 1992, **97**, 2571–2577.
66 J. S. Binkley, J. A. Pople and W. J. Hehre, *J. Am. Chem. Soc.*, 1980, **102**, 939–947.
67 W. J. Stevens, H. Basch and M. Krauss, *J. Chem. Phys.*, 1984, **81**, 6026–6033.
68 R. Cundari and W. J. Stevens, *J. Chem. Phys.*, 1993, **98**, 5555–5565.
69 R. Dennington, T. A. Keith and J. M. Millam, Semichem Inc., Shawnee Mission, Kansas, USA, 2016.

 This journal is © The Royal Society of Chemistry 2021